

Influence of the skew angle on the hydroelastic behaviour of a composite marine propeller

Hassan Ghassemi¹, Maryam Gh Saryazdi² and Morteza Ghassabzadeh¹

Abstract

This paper discusses the influence of the skew angle on the hydroelastic behaviour of a composite marine propeller. Recently, propellers have been made of composite materials because of their useful acoustic properties and because they are lightweight. However, the flexibility of composites causes much deflection in comparison with conventional materials and a change in the hydroelastic performances of propellers. In this research, the hydroelastic behaviour of a propeller is analysed for various skew angles using the prepared software code, namely the boundary element method–finite element method hydroelastic code, in which the hybrid boundary element method–finite element method is used. The hydrodynamic load acting on the propeller is determined by the boundary element method, and the deformed propeller is then obtained by the finite element method. The iterations between the boundary element method and the finite element method are repeated until the deflection and hydrodynamic characteristics (the thrust, the torque and the efficiency) of the propeller converged. The numerical results indicate that the skew angle affects the performance of the propeller and the stress field. As the skew angle increases, the maximum deflection of the blade increases; however, the thrust coefficient and the torque coefficient decrease.

Keywords

Hydro-elastic analysis, skew angle, propeller characteristics, flexible blade

Date received: 20 November 2011; accepted: 1 February 2012

Introduction

Hydroelasticity is a problem concerned with the interactions of deformable bodies with the water environment in which they operate. Most structural bodies are naturally flexible and undergo strains and stresses, especially composite materials. The applications of such materials are demanded in the design of numerous marine elements. The marine propeller is an efficient element that may be constructed from composite material because of its useful acoustic properties and its high strength-to-weight ratio. It operates behind the ship's stern to generate thrust, from the pressure load acting on the blade, to drive the marine vehicle. Because of the loading on the propeller, its reaction may be significant in the performance obtained from hydroelastic analysis. The study of the effect of deformation on the performance of the propeller may be an interesting topic for researchers, in order to optimize the propeller design.^{1,2}

Until now, the hydroelastic behaviours of propellers has been treated by a number of researchers by different

methodologies. Sontvedt³ obtained the results from application of shell elements to calculate the quasi-static and dynamic stresses in marine propeller blades. Young⁴ presented a coupled boundary element method (BEM)–finite element method (FEM) for numerical analysis of flexible composite propellers in uniform flow and in wake inflow. The fluid–structure interaction analysis of flexible composite marine propellers subject to hydrodynamic and inertial loads was also presented by Young.⁵ Recently, numerical analysis of a large-scale surface-piercing propeller (SPP) was reported by Young and Savander.⁶ They presented three SPP

¹Department of Marine Technology, Amirkabir University of Technology, Tehran, Iran

²Department of Mechanical Engineering, Science and Research Branch, Islamic Azad University, Tehran, Iran

Corresponding author:

Hassan Ghassemi, Department of Marine Technology, Amirkabir University of Technology, Hafez Avenue, PO Box 424, 15875-4413 Tehran, Iran.
Email: gasemi@aut.ac.ir

designs for surface-effect ships of different sizes, which can attain a maximum speed of advance of 50 kn. A coupled structural–fluid flow analysis was performed by Blasques et al.⁷ to evaluate the hydroelastic behaviour of a composite marine propeller. An MAU propeller was analysed with different stacking sequences of composite lay-up. The hydroelastic behaviours of the propeller with balanced and unbalanced stacking sequences were investigated and discussed by Lin et al.⁸ Mulcahy et al.⁹ carried out comprehensive work on the hydroelastic tailoring of a flexible composite propeller. The blade stress–strain curves of a marine propeller were analysed by Chau.¹⁰ Koronowicz et al.¹¹ prepared a comprehensive computer program to treat the hull propeller–rudder system in the process of propeller design. The program outcomes included the hydrodynamic performance, the cavitation effect, the blade strength and optimization of the efficiency.

A ship propeller design (SPD) software code was prepared by Ghassemi and employed for various propulsors such as a propeller–rudder system,¹² a highly skewed propeller,¹³ a contra-rotating propeller¹⁴ and an SPP.¹⁵ This code employs the BEM including the boundary layer theory to determine the hydrodynamic analysis of a marine propeller.

In this article, the influence of the skew angle on the hydroelastic performance of a composite propeller is studied using coupled BEM–FEM analysis. The shape of the propeller may be determined by an iterative method, in which the hydrodynamics forces acting on the blades are calculated by modelling the fluid–structure interaction in a boundary element code. The deformation of the blades is then calculated using a finite element model. The geometry of the deformed propeller is determined for four skew angles and the effect of the deformation on the propeller’s performance is examined for several values of the advance

coefficient. The following sections are organized as follows. The methodology details of the BEM–FEM hydroelastic code are described in the second section. Numerical results and a discussion are presented in the third section. Finally, the fourth section gives the conclusions.

BEM–FEM hydroelastic code

In this paper, the BEM–FEM hydroelastic code is developed to examine the hydroelastic performance of a flexible propeller. In this code, the boundary element techniques and boundary layer theory are used to determine the hydrodynamic pressure. By development of a macro, the blade geometry is generated automatically in the FEM code. The hydrodynamic pressure is applied to the finite element model and the deformed blade is determined by structural analysis. Until the selected parameters converge, the iteration between BEM and FEM proceeds.

For a discussion of the propeller geometry at a global right angle, a rectangular Cartesian system is chosen, as depicted in Figure 1(a). The X axis is positive, forward and coincident with the shaft axis, the Y axis is positive to starboard and the Z axis is positive in the vertically downward direction. For the propeller geometry, a local reference frame having a common axis such that OX and Ox are coincident but allowing the mutually perpendicular axes Oy and Oz to rotate relative to the OY and OZ fixed global frame is also defined.

Based on the International Towing Tank Conference (ITTC) code, the skew angle $\theta_s(x)$ of a particular section (Figure 1(b)) is defined as the angle between the propeller reference line (directrix) and a line drawn through the shaft centre-line and the mid-chord point of a

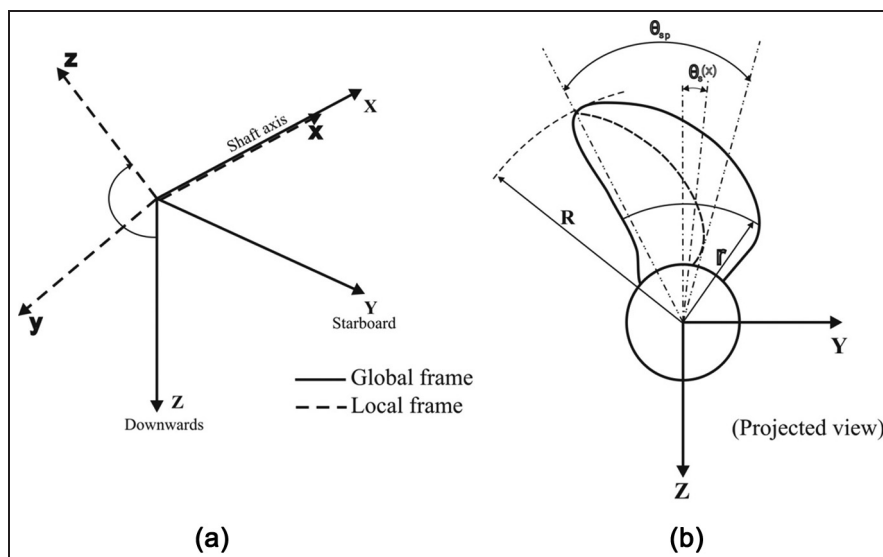


Figure 1. (a) Global and local coordinate system; (b) skew angle of the propeller.

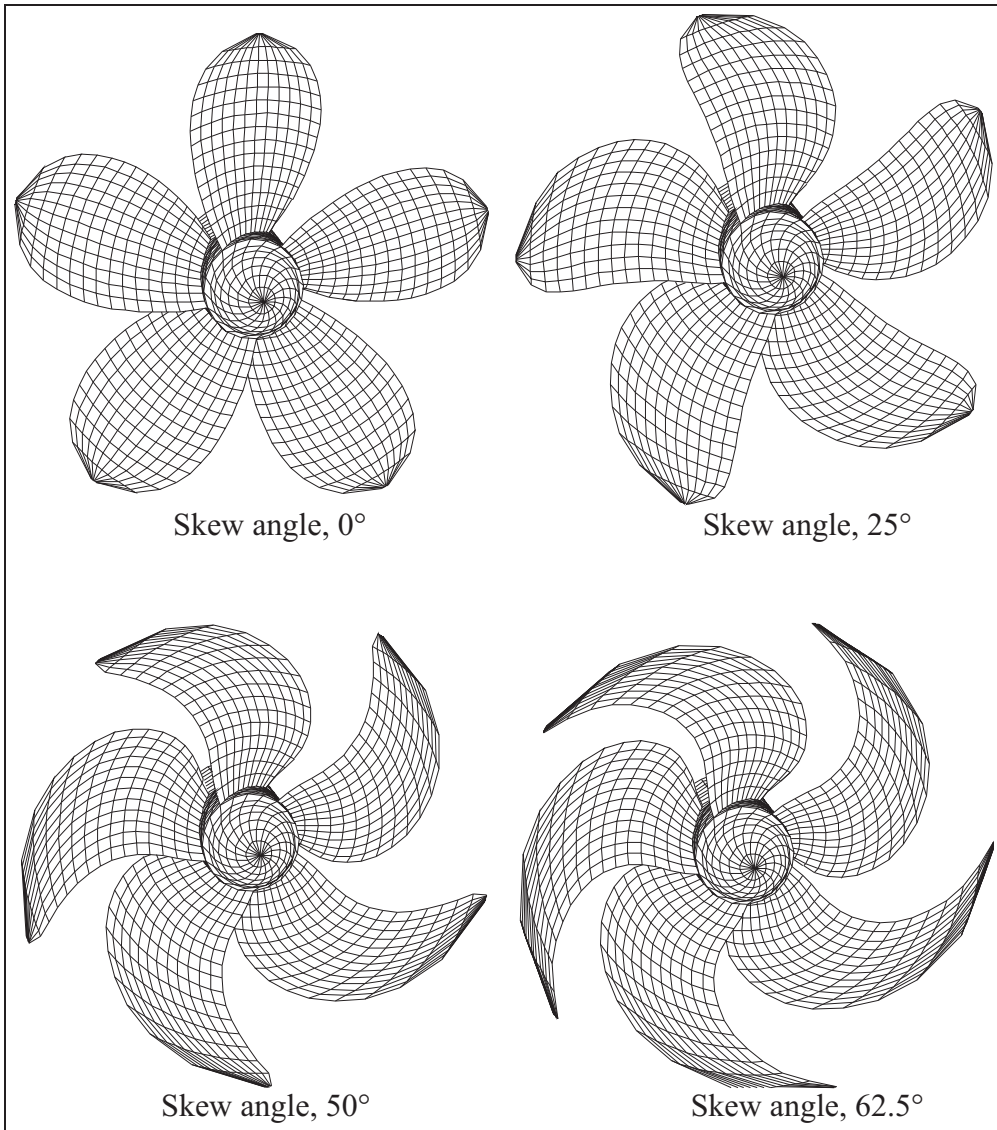


Figure 2. Mesh surface of the undeformed propellers at four skew angles in the BEM code.

section (in the $y-z$ plane) at its non-dimensional radius $x (= r/R)$ in the projected plane. The propeller skew angle θ_{sp} is defined as the largest angle, measured at the shaft centre-line, in the projected plane, which can be drawn between lines passing from the shaft centre-line through the mid-chord position of any two sections.

Boundary element theory for hydrodynamic analysis

The boundary element method is based on Green's theory in which the governing equations of the volume domain are transferred to the boundary of the body. Therefore, in three-dimensional problems, the surface elements may be used to analyse the model.

In the BEM code, considering the motion of a body in a real incompressible fluid, the thrust and torque of the propeller are calculated using the hydrodynamic pressure and the shear forces. The thrust is almost entirely due to the hydrodynamic pressure which is

determined by the BEM. However, the torque is calculated on the basis of the ITTC empirical formulae. The potential theory is employed to determine the pressure distribution. In the BEM software code the boundary surface of the propeller is discretized into quadrilateral elements (Figure 2). The boundary value problems should then be applied to determine the velocity potential. Since the propeller is a lifting body, the Kutta condition should be satisfied as an essential boundary condition for the propeller. Using the boundary element techniques and the boundary layer theory,¹³ the hydrodynamic pressure P_h and the tangential stress τ are determined as

$$\begin{aligned} P_h &= 0.5\rho \left(2\vec{V}_R \cdot \nabla\phi - \nabla\phi \cdot \nabla\phi \right) \\ \tau &= 0.5\rho C_f \vec{V}_R^2 \end{aligned} \quad (1)$$

where $\nabla\phi$ is the derivative of the velocity potential, ρ is the density of water, C_f is the frictional coefficient

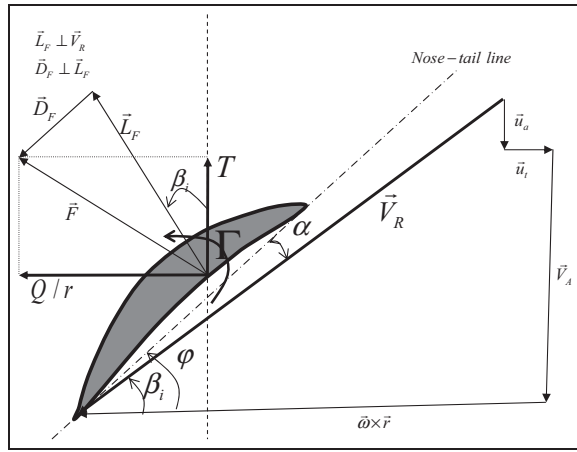


Figure 3. Inflow velocity and hydrodynamic forces acted on the blade at radius r .

which is determined by the ITTC empirical formulae and \vec{V}_R is the inflow velocity, in the case of the propeller, which is calculated as

$$\vec{V}_R = (\vec{V}_A + \vec{u}_a) + (\vec{\omega} \times \vec{r} - \vec{u}_t) \quad (2)$$

Here, $\vec{\omega}$ and \vec{V}_A are the rotational velocity and advance velocity, respectively. The rotational speed of propeller is obtained by $n = \frac{|\vec{\omega}|}{2\pi}$ (RPS). \vec{u}_a and \vec{u}_t are the axial and tangential induced velocities respectively, which are determined by the derivative of velocity potential. Figure 3 shows the velocity vectors and the hydrodynamic forces acting on the blade at radius r . All the parameters that are shown in Figure 3 are listed in the notation in Appendix 1.

The total thrust T and torque Q of the propeller are determined as

$$\begin{aligned} T &= \int_S P_h n_x \, dS + \int_S \tau n_x \, dS \\ Q &= \int_S P_h r(n_y z - n_z y) \, dS - \int_S \tau r(n_y z - n_z y) \, dS \end{aligned} \quad (3)$$

respectively, where \vec{n} is the normal vector of the element surface with the components (n_x, n_y, n_z) .

The non-dimensional hydrodynamic coefficients (the thrust coefficient K_T , the torque coefficient K_Q and the efficiency η) of the propeller are expressed as

$$\begin{aligned} K_T &= \frac{T}{\rho n^2 D^4} \\ K_Q &= \frac{Q}{\rho n^2 D^5} \\ \eta &= \frac{J}{2\pi} \frac{K_T}{K_Q} \end{aligned} \quad (4)$$

where D is the propeller diameter. The advance velocity ratio J is determined as

$$J = \frac{V_A}{nD} \quad (5)$$

Finite element theory for structural analysis

The finite element code is used for structural analysis of the propeller. A macro is generated and imported to the FEM code in which the blade geometry is generated automatically using the general characteristics of the propeller. The boundary conditions and loads are then applied to the propeller. The FEM model of the propeller is analysed and the results data are exported to the output file. In the generated macro, the geometry model is meshed regularly with the three-dimensional solid element with 20 nodes. The finite element model is created according to the x , y and z coordinates of the nodes used in the BEM model. Therefore the results of the FEM can be transferred to the BEM code simply.

It is assumed that the propeller is made of a linear elastic orthotropic material. There are nine independent elastic constants associated with the orthotropic material. The relation between the strain ε and the stress σ is presented as

$$\left\{ \begin{array}{l} \varepsilon_x \\ \varepsilon_y \\ \varepsilon_z \\ \gamma_{xy} \\ \gamma_{xz} \\ \gamma_{yz} \end{array} \right\} = \left[\begin{array}{cccccc} \frac{1}{E_x} & \frac{-\nu_{xy}}{E_y} & \frac{-\nu_{xz}}{E_z} & 0 & 0 & 0 \\ \frac{-\nu_{xy}}{E_x} & \frac{1}{E_y} & \frac{-\nu_{yz}}{E_z} & 0 & 0 & 0 \\ \frac{-\nu_{xz}}{E_x} & \frac{-\nu_{yz}}{E_y} & \frac{1}{E_z} & 0 & 0 & 0 \\ 0 & 0 & 0 & \frac{1}{G_{xy}} & 0 & 0 \\ 0 & 0 & 0 & 0 & \frac{1}{G_{xz}} & 0 \\ 0 & 0 & 0 & 0 & 0 & \frac{1}{G_{yz}} \end{array} \right] \left\{ \begin{array}{l} \sigma_x \\ \sigma_y \\ \sigma_z \\ \tau_{xy} \\ \tau_{xz} \\ \tau_{yz} \end{array} \right\} \quad (6)$$

where E , G and ν are the modulus of elasticity, the shear modulus of elasticity and Poisson's ratio respectively.

In the global frame (Figure 1(a)), the discrete equation of motion can be written as

$$[M]\{\ddot{u}\} + [C]\{\dot{u}\} + [K]\{u\} = \{F_{ce}\} + \{F_P\} + \{F_g\} \quad (7)$$

where $[\ddot{u}]$, $[\dot{u}]$ and $[u]$ are the acceleration vector, the velocity vector and the displacement vector respectively. $[M]$, $[C]$ and $[K]$ are the structural mass matrix, the damping matrix and the stiffness matrix respectively. $\{F_{ce}\}$ is the centrifugal force vector calculated for each element from the equation

$$f_{ce} = \int_v \rho_b r_e n^2 \, dv \quad (8)$$

where r_e is the radial position of the centre of the element, ρ_b is the density of the blade and n is the rotational speed of the propeller (Figure 4). $\{F_g\}$ is the force vector due to gravity calculated for each element from the equation

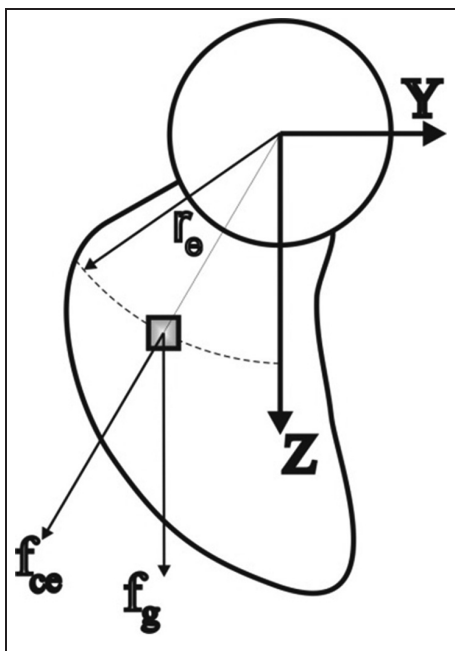


Figure 4. Direction of the force due to gravity and the centrifugal force.

$$f_g = \int_v \rho_b g \, dv \quad (9)$$

$\{F_P\}$ represents the sum of the hydrodynamic forces and the hydrostatic forces which are given by

$$f_P = \int_A P \, dA \quad (10)$$

P , the total pressure of each element, is determined as

$$P = P_h + P_0 + \rho g(Y_{CE} + H) \quad (11)$$

where P_0 is the atmospheric pressure, H is the depth of the hub below the free surface and Y_{CE} is the position of the element centre in the Y direction. The hydrodynamic pressure P_h is calculated by the BEM code and imported to the FEM.

It is clear that the loading conditions of the blades depend on their positions. In every revolution, the maximum load is applied to each blade once. In the vertical and downward position, the critical load is applied to each blade. In this situation, the force due to gravity and the centrifugal force are in the same direction. In addition, the summation of the atmospheric pressure, the hydrostatic pressure (due to the head of water above the hub) and the hydrodynamic pressure are applied on the surface blade.

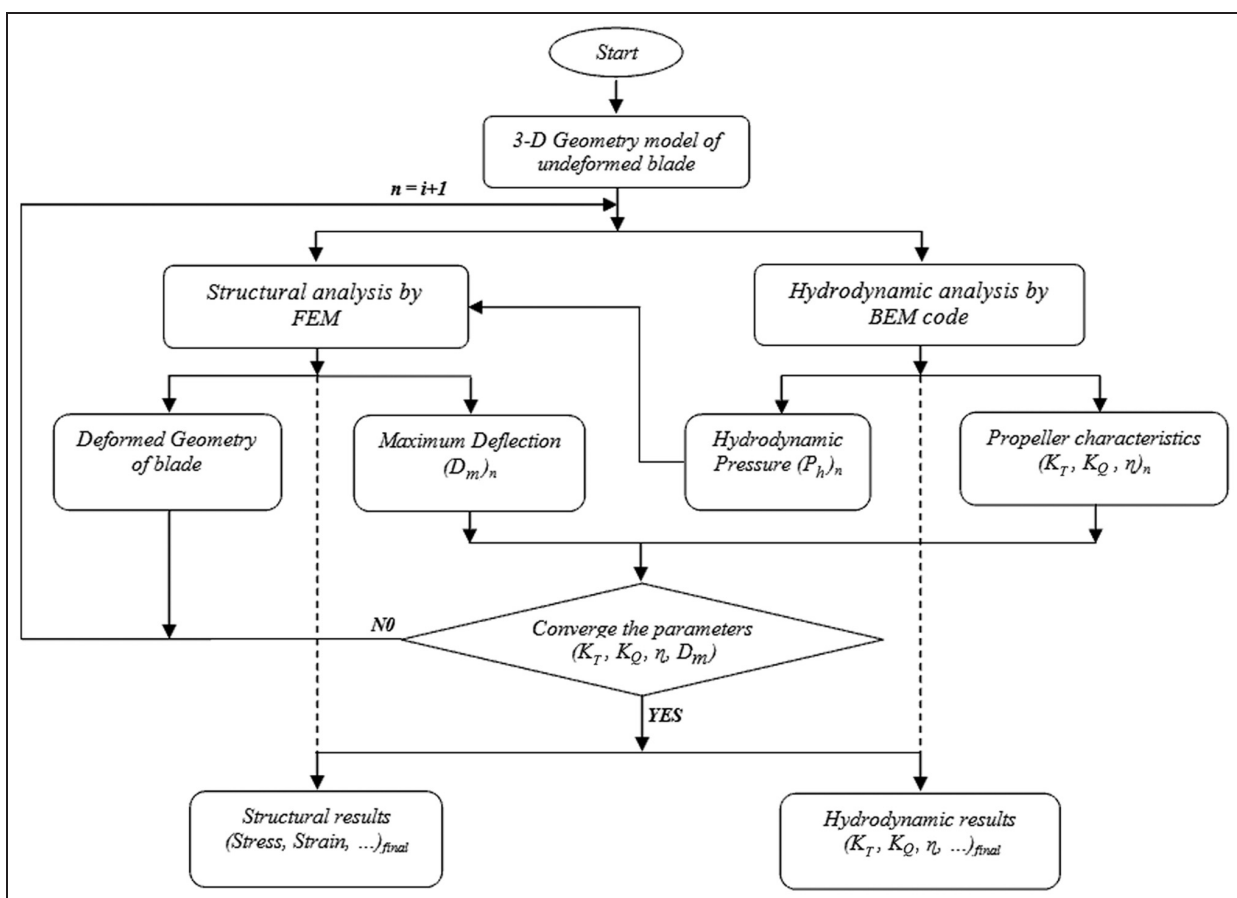


Figure 5 Flow chart of the computational proposed method.
3-D: three-dimensional.

Table 1. Main dimensions of the propeller.

Parameter	Value
Number of blades Z	5
Diameter (m)	0.70
Hub ratio r_h/R	0.2
Pitch ratio P/D	Variable
Expanded area ratio	0.65
Skew angle (deg)	Variable
Rake angle (deg)	10

Table 2. The pitch ratios, chord ratios and thickness ratios of the propeller.

Radial section r/R	Thickness ratio t_{max}/D	Chord ratio C/D	Pitch ratio P/D
0.2	0.052983	0.295593	0.64
0.24	0.05047	0.316279	0.659345
0.28	0.048014	0.335838	0.679659
0.32	0.045574	0.354183	0.700361
0.36	0.043135	0.371214	0.720748
0.4	0.040686	0.38682	0.74
0.44	0.038237	0.400906	0.757436
0.48	0.035792	0.413426	0.772951
0.52	0.033353	0.42434	0.786596
0.56	0.030912	0.43342	0.798727
0.6	0.028449	0.440247	0.81
0.64	0.025947	0.444264	0.820521
0.68	0.02353	0.4444	0.828135
0.72	0.021094	0.43948	0.830227
0.76	0.018629	0.428926	0.826707
0.8	0.01616	0.412759	0.82
0.84	0.013704	0.389676	0.811624
0.88	0.011258	0.352983	0.799014
0.92	0.008851	0.294136	0.778841
0.96	0.006436	0.193052	0.753691
1	0.003915	0.022132	0.73

The procedure of the proposed method

The flow chart of the computational proposed method is presented in Figure 5. First, the undeformed blade is analysed in the HYDRO-BEM software code to determine the hydrodynamic forces, the efficiency, K_T and K_Q , for which the fluid–structure interaction is considered. The deformations of the blade are then determined using the ELASTIC-FEM software code. In the second step, the hydrodynamic forces, the efficiency, K_T and K_Q are determined on the basis of the deformed shape of the blade in the BEM code. The deformations of the blade are calculated in the FEM software again based on the new calculated hydrodynamic forces. Comparing the results of the two steps, the convergence of the selected parameters (the maximum deflection, the efficiency, K_T and K_Q) is checked. The procedure is performed until convergence of the selected parameters. In the final step, the deformed shape of the blade and the other parameters are calculated.

Table 3. The material properties of the propeller.

Modulus of elasticity (GPa)	Poisson's ratio	Shear modulus of elasticity (GPa)
$E_x = 132$	$\nu_{xy} = 0.24$	$G_{xy} = 5.65$
$E_y = 10.8$	$\nu_{yz} = 0.49$	$G_{yz} = 3.38$
$E_z = 10.8$	$\nu_{xz} = 0.24$	$G_{xz} = 5.65$

Numerical results and discussion

In this study, a five-bladed propeller is selected to examine the effect of deformation on the propeller's performance. The analysis is carried out for the four skew angles 0° , 25° , 50° and 55° . The main dimensions of the propeller are listed in Table 1. The thickness ratios, chord ratios and pitch ratios of the propeller for different values of r/R are given in Table 2.

The material properties of the propeller are listed in Table 3.¹⁶ It is assumed that the propeller is made of linear elastic anisotropic composite laminates stacked in the thickness direction.

In the FEM analysis, for simplicity and to save time, one blade of the propeller is modelled. It is assumed that the root of the blade is fixed. The forces acting on the propeller included the hydrodynamic loads (i.e. the thrust and the torque), the centrifugal force and the force due to gravity. In the vertical and downward position, the maximum force is acting on the blade because the centrifugal force and the force due to gravity are in the same direction.

The model of the blade geometry is shown in Figure 6. Because of the complexity of the blade shape, the geometry of the blade is divided into several volumes. This helps to create an accurate model of the blade geometry. To achieve grid independence of the model, several FEM models are created with different element sizes. The size of the elements is reduced stepwise until the results converged to the same after a specific step. Figure 7 shows the finite element model of the blade. Because of the complexity of the tip geometry and the sudden reduction in the blade section (especially for large skew angles), the elements of the blade tip are refined in this region.

Based on the flow chart presented in Figure 5, the three-dimensional model of the undeformed blade is analysed in the HYDRO-BEM code to calculate the hydrodynamic pressure. The results are then exported to the ELASTIC-FEM software to calculate the deformation of the blade. This procedure is repeated until the maximum deformation, the efficiency, the thrust coefficient and the torque coefficient converge. The hydroelastic analysis of each blade is carried out for eight advance velocity ratios $J = 0.2\text{--}0.9$ in steps of 0.1. The results show that the propeller is under more loading at $J = 0.2$. Therefore, most of the results are plotted for $J = 0.2$.

Figure 8 shows the convergence of the parameters (K_T , $10K_Q$ and the efficiency) for a skew angle of 55° at

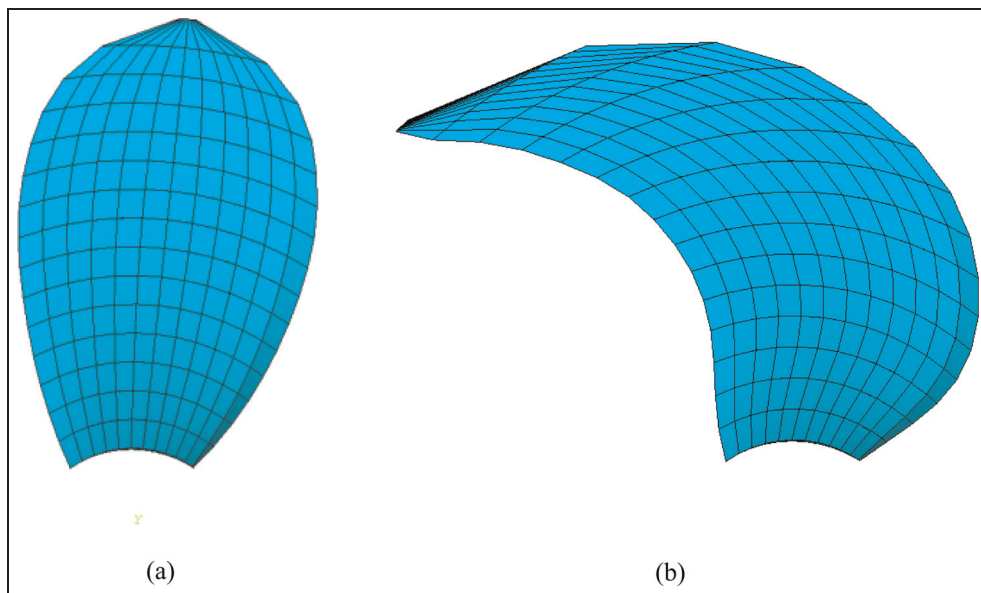


Figure 6. Geometry model of the blade in the FEM code: (a) $\theta_{sp} = 0^\circ$; (b) $\theta_{sp} = 55^\circ$.

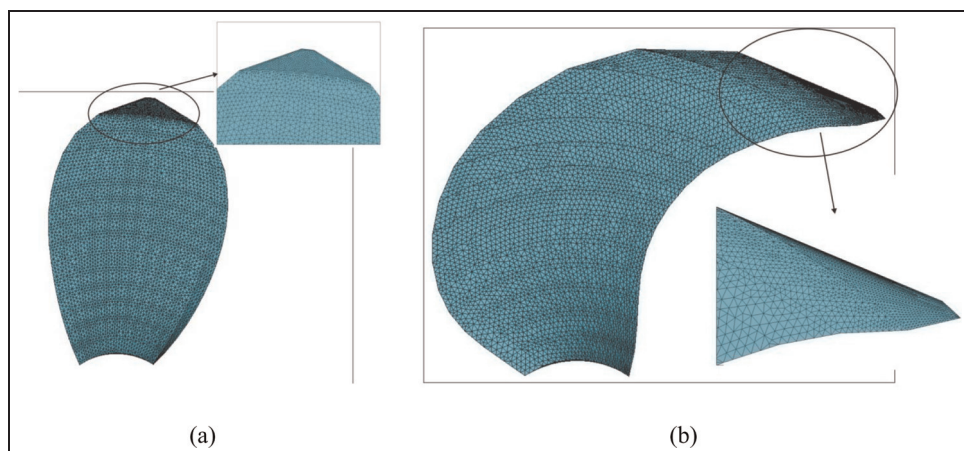


Figure 7. Finite element model of the blade: (a) $\theta_{sp} = 0^\circ$; (b) $\theta_{sp} = 55^\circ$.

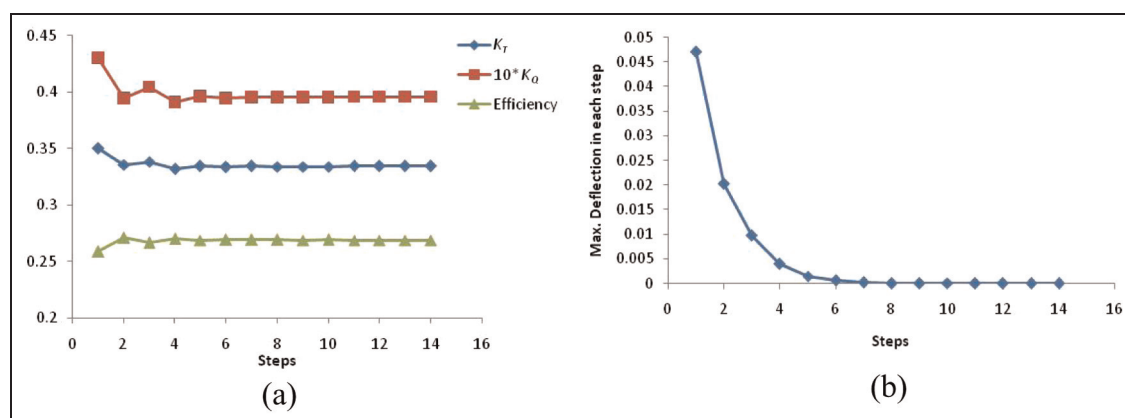


Figure 8. Convergence steps for a skew angle of 55° at $J = 0.2$: (a) K_T , K_Q and efficiency; (b) maximum deflection.

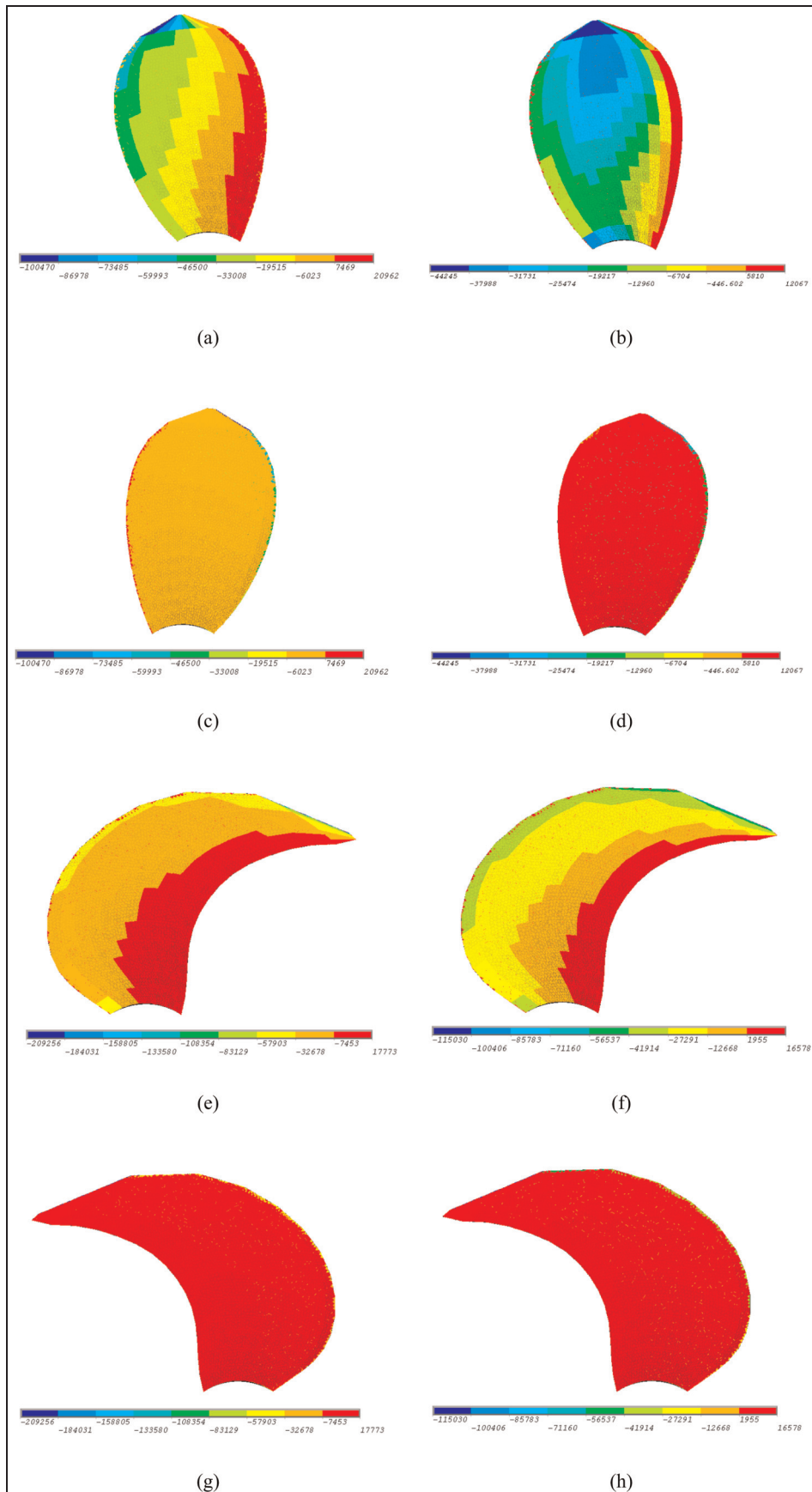


Figure 9. Hydrodynamic pressure distributions on the face and the back of the undeformed and deformed blades at $J=0.2$: (a) $\theta_{sp}=0^\circ$, face of the undeformed blade; (b) $\theta_{sp}=0^\circ$, face of the deformed blade; (c) $\theta_{sp}=0^\circ$, back of the undeformed blade; (d) $\theta_{sp}=0^\circ$, back of the deformed blade; (e) $\theta_{sp}=55^\circ$, face of the undeformed blade; (f) $\theta_{sp}=55^\circ$, face of the deformed blade; (g) $\theta_{sp}=55^\circ$, back of the undeformed blade; (h) $\theta_{sp}=55^\circ$, back of the deformed blade.

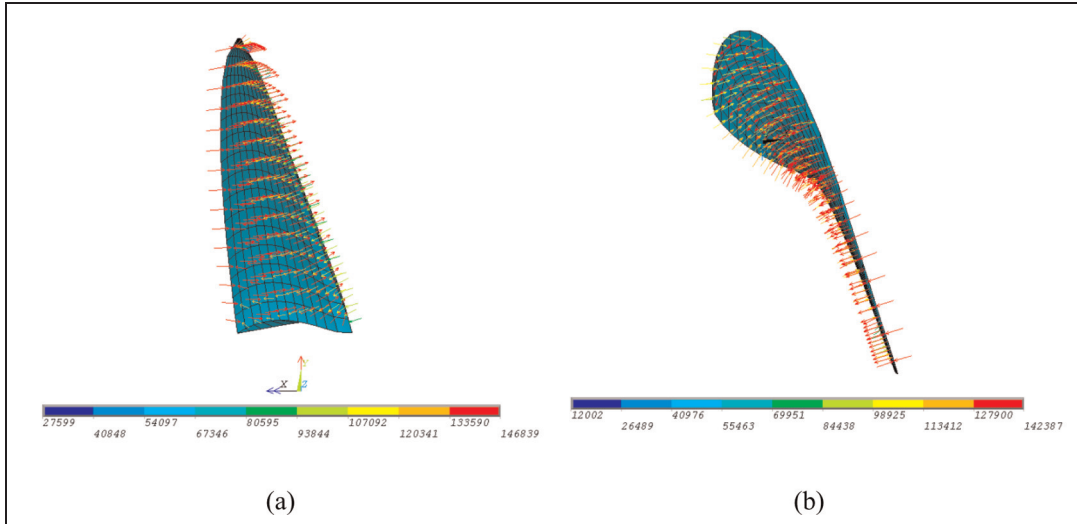


Figure 10. Total pressure on the blade at $J=0.2$: (a) $\theta_{sp}=0^\circ$; (b) $\theta_{sp}=55^\circ$.

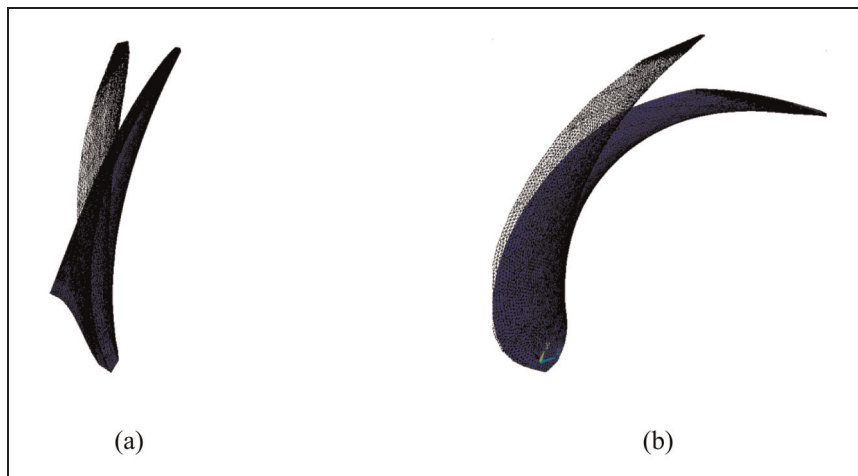


Figure 11. Undeformed and deformed shapes of the blade at $J=0.2$: (a) $\theta_{sp}=0^\circ$; (b) $\theta_{sp}=55^\circ$.

$J = 0.2$. The variations in the parameters almost vanished after six steps of hydroelastic analysis and after eight steps for deflection.

Figure 9 shows the hydrodynamic pressure distributions on the faces and the backs of the undeformed and deformed blades for skew angles of 0° and 55° at $J = 0.2$. It is clear that the deformation of the blade affects the pressure distribution. The hydrodynamic pressure of the deformed blade is less than that of the undeformed blade. The vector of the total pressure distribution on the surface of blade is shown in Figure 10 at $J = 0.2$ for $\theta_{sp} = 0^\circ$ and $\theta_{sp} = 55^\circ$.

The deformed and undeformed shapes of the blade, on a scale of 10, for $\theta_{sp} = 0^\circ$ and $\theta_{sp} = 55^\circ$ at $J = 0.2$ are illustrated in Figure 11. It is shown that the deformation of the blade with $\theta_{sp} = 55^\circ$ is greater than the deformation of the blade with $\theta_{sp} = 0$. The deformation fields of the blade for skew angles of 0° and 55° at $J = 0.2$ are shown in Figure 12. The deformation

increases towards the blade tip owing to the increase in the centrifugal force, the hydrodynamic pressure and the cantilever-like behaviour of the blade.

Figure 13 shows the maximum principal stress at the face of blade at $J = 0.2$ for four skew angles. The maximum principal stress occurs in the middle of the blade root. For $\theta_{sp} = 0^\circ$ and $\theta_{sp} = 25^\circ$, the stress near the edges is about 10% of the maximum stress. However, for $\theta_{sp} = 50^\circ$ and $\theta_{sp} = 55^\circ$, the stress near the edges is about 65% of the maximum stress.

The maximum principal stress σ_1 , the normal stress σ_x in the x direction and the shear stress τ_{yz} versus the skew angle are shown in Figure 14. It is observed that the maximum value of σ_1 and σ_x occur at a skew angle of 25° . With increasing skew angle, the shear stress slightly increases. Figure 15 shows the maximum deflection of the blade versus the advance velocity ratio J for different skew angles. For each value of the advance velocity ratio, the maximum deflection appears at the

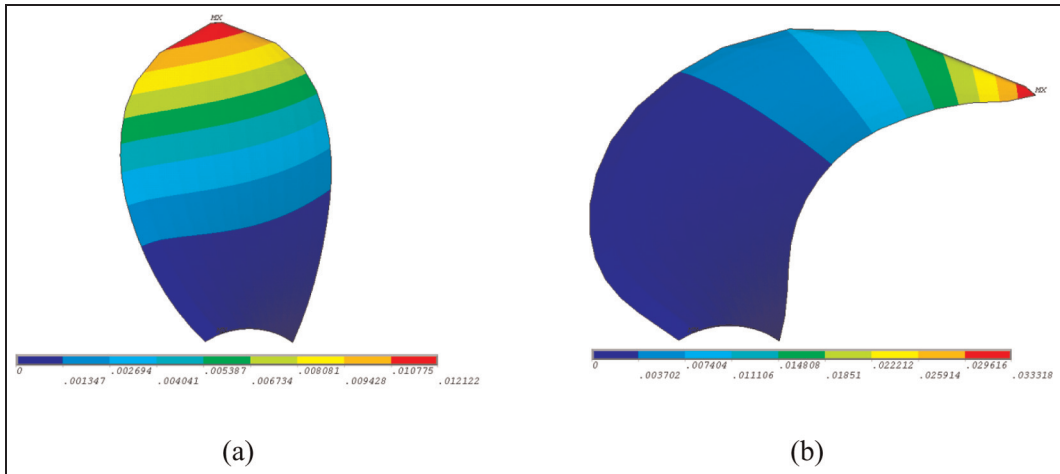


Figure 12. Deformation of the blade at $J=0.2$: (a) $\theta_{sp}=0^\circ$; (b) $\theta_{sp}=55^\circ$.

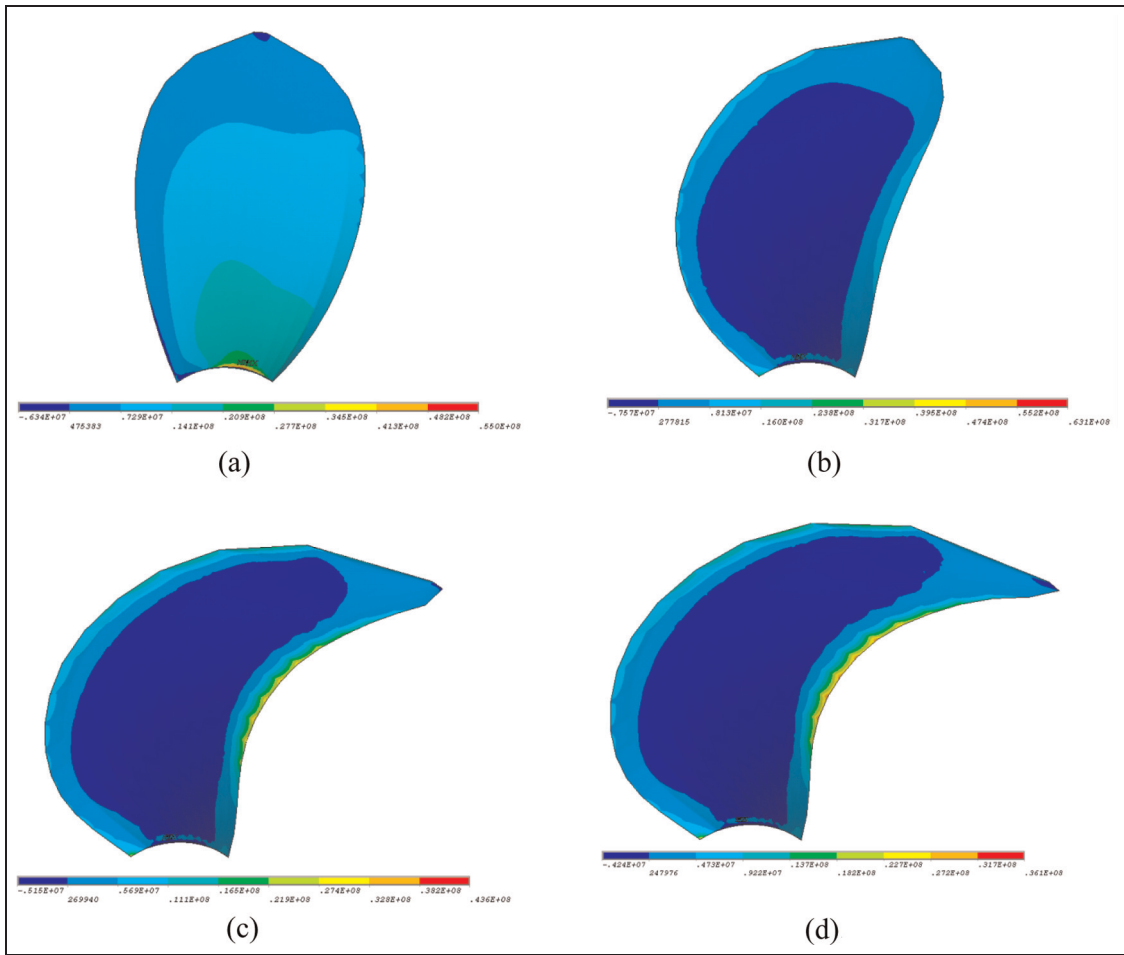


Figure 13. Maximum principal stress of blade at $J = 0.2$: (a) $\theta_{sp} = 0^\circ$; (b) $\theta_{sp} = 25^\circ$; (c) $\theta_{sp} = 55^\circ$; (d) $\theta_{sp} = 62.5^\circ$.

maximum value of the skew angle. When the advance velocity ratio increases, the maximum deflection of the blade decreases. Therefore the maximum deflection, for each value of skew angle, occurs at $J = 0.2$.

The thrust coefficient of the deformed blade versus the advance velocity ratio is shown in Figure 16 for various skew angles. It is shown that a larger skew angle gives a lower performance of the thrust for each value

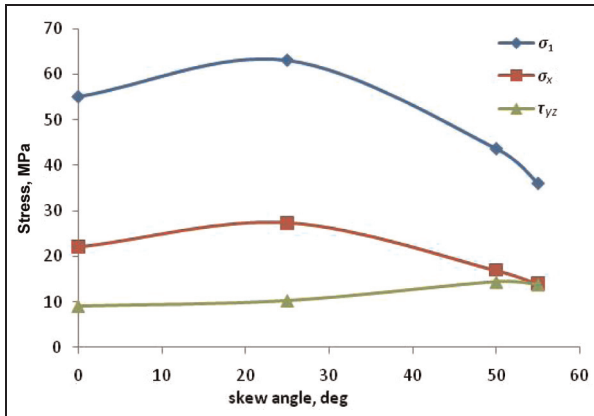


Figure 14. Stress versus the skew angle at $J = 0.2$ (σ_1 is the maximum principal stress, σ_x is the normal stress in the x direction and τ_{yz} is the shear stress).

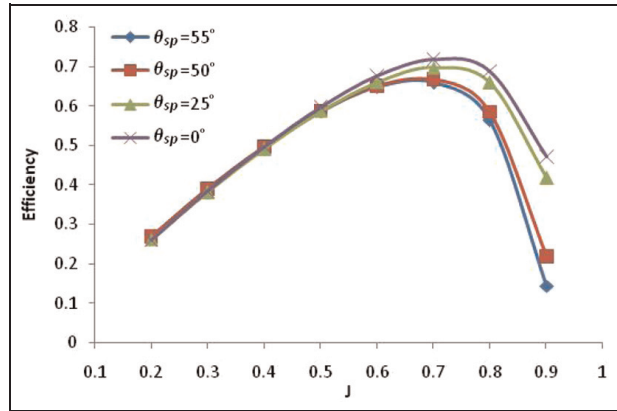


Figure 17. Efficiency of the deformed blade versus the advance velocity ratio.

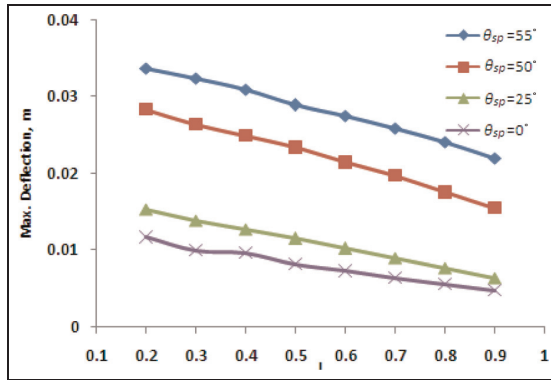


Figure 15. Maximum deflection of the blade versus the advance velocity ratio.

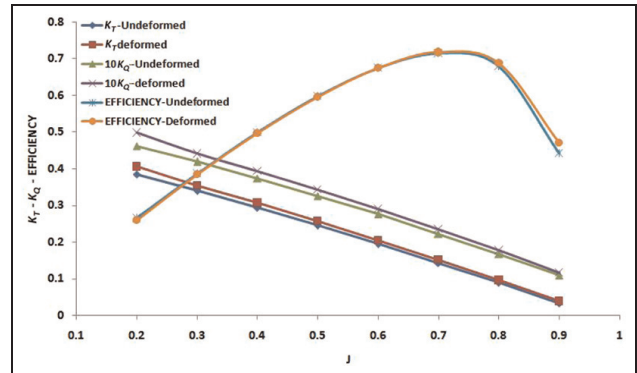


Figure 18. Hydrodynamic characteristics of the undeformed and deformed propellers ($\theta_{sp} = 0^\circ$).

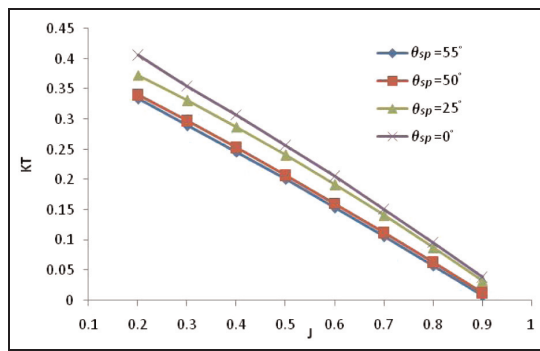


Figure 16. Thrust coefficient of the deformed blade versus the advance velocity ratio.

of the advance velocity ratio. Furthermore the thrust coefficient decreases with increasing advance velocity ratio.

Figure 17 shows the efficiency of the propeller versus the advance velocity ratio J for various skew angles.

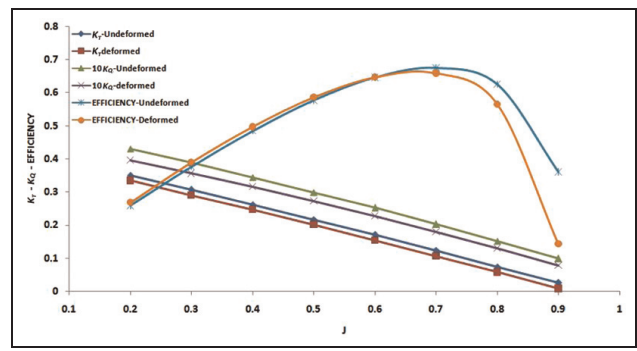


Figure 19. Hydrodynamic characteristics of the undeformed and deformed propellers ($\theta_{sp} = 55^\circ$).

The maximum efficiency occurs at $J = 0.7$ for skew angles of 50° and 55° ; however, for skew angles of 0° and 25° , the maximum value of the efficiency shifts slightly to a higher advance velocity ratio. For $J < 0.5$, the curves are similar but, for $J > 0.5$, the efficiency

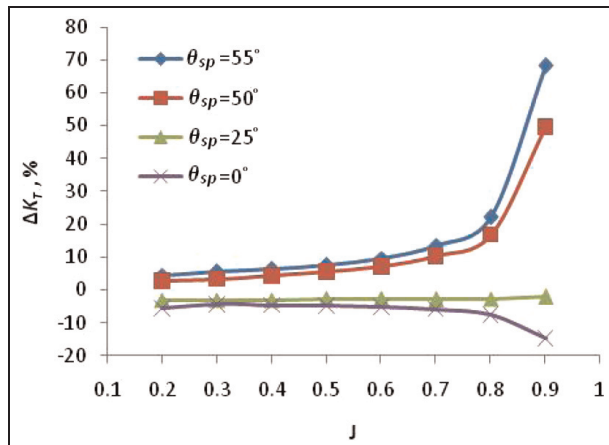


Figure 20. Relative variation in the thrust coefficient versus the advance velocity ratio.

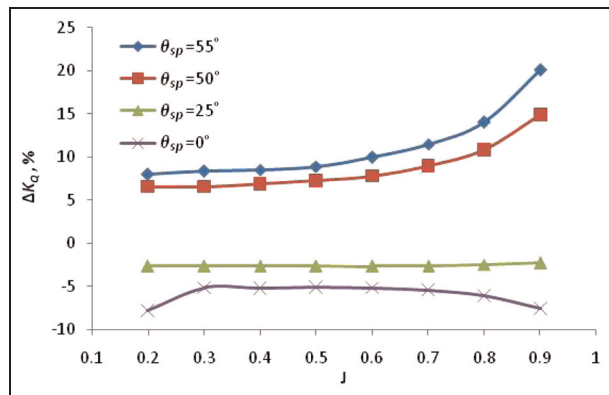


Figure 21. Relative variation in the torque coefficient versus the advance velocity ratio.

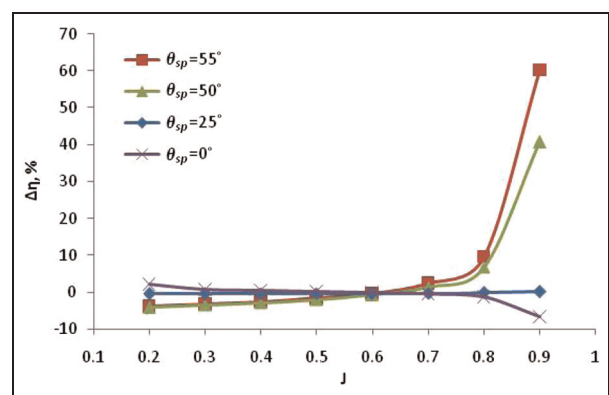


Figure 22. Relative variation in the efficiency versus the advance velocity ratio.

decreases with increasing skew angle for each value of the advance velocity ratio.

Figure 18 and Figure 19 show the hydrodynamic characteristics (K_T , K_Q and the efficiency) of deformed and undeformed propeller blades versus the advance velocity ratio for two skew angles $\theta_{sp} = 0^\circ$ and $\theta_{sp} = 55^\circ$ respectively. For $\theta_{sp} = 0^\circ$, the efficiency of the

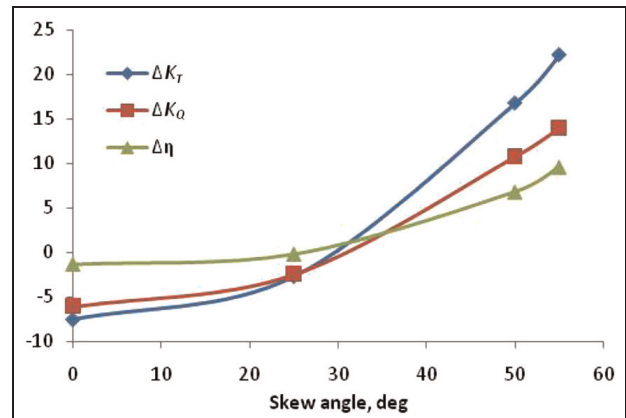


Figure 23. Relative variations in the hydrodynamic characteristics versus the skew angle at $J = 0.8$.

deformed blade is nearly equal to that of the undeformed blade up to $J = 0.7$ (Figure 18). For $\theta_{sp} = 55^\circ$, the efficiency of the deformed blade is higher than that of the undeformed blade for $J < 0.6$; however, for $J > 0.6$ the converse is true (Figure 19). For $\theta_{sp} = 0^\circ$, K_T and K_Q for the deformed blade are higher than the corresponding values for the undeformed blade but in the opposite way to those for $\theta_{sp} = 55^\circ$.

In order to examine the effect of the skew angle on the hydrodynamic characteristics precisely, the variations in the propeller characteristics relative to those of the undeformed blade are defined as

$$\begin{aligned}\Delta K_{Tr} &= \frac{K_T - K_{T0}}{K_{T0}} \times 100 \\ \Delta K_{Qr} &= \frac{K_Q - K_{Q0}}{K_{Q0}} \times 100 \\ \Delta \eta_r &= \frac{\eta - \eta_0}{\eta_0} \times 100\end{aligned}\quad (12)$$

where the subscript 0 indicates the undeformed blade.

Figure 20, Figure 21 and Figure 22 represent the variations in ΔK_{Tr} , ΔK_{Qr} and $\Delta \eta_r$ respectively versus J for various skew angles. For $\theta_{sp} = 25^\circ$, the relative variations in the propeller characteristics are nearly constant ($\Delta \eta_r$ is equal to nearly zero), and so the performance of the propeller is independent of the rotational speed and the advance velocity. For $\theta_{sp} = 0^\circ$, the variations in ΔK_{Tr} and ΔK_{Qr} versus J are negative and very similar to a convex shape. However, for $\theta_{sp} = 50^\circ$ and $\theta_{sp} = 55^\circ$, ΔK_{Tr} and ΔK_{Qr} are positive and increase with increasing advance velocity ratio. ΔK_{Tr} increases slightly and reaches 20% at $J = 0.8$ but jumps to 60% at $J = 0.9$. For $\theta_{sp} = 0^\circ$, $\Delta \eta_r$ is positive at $J < 0.6$ and negative at $J < 0.6$; however, the opposite situation occurs for $\theta_{sp} = 50^\circ$ and $\theta_{sp} = 55^\circ$.

In order to show the effect of the skew angle, plots of ΔK_{Tr} , ΔK_{Qr} and $\Delta \eta_r$ versus the skew angle (at a typical value, i.e. $J = 0.8$) are shown in Figure 23. For $\theta_{sp} < 30^\circ$, ΔK_{Tr} , ΔK_{Qr} and $\Delta \eta_r$ are negative and, for $\theta_{sp} > 30^\circ$, they are positive. When the skew angle increases, ΔK_{Tr} , ΔK_{Qr} and $\Delta \eta_r$ increase. It is found that

the effect of the skew angle on $\Delta\eta_r$ is less than the effects on ΔK_{Tr} and ΔK_{Qr} .

Conclusions

A flexible marine propeller is analysed using the hydro-elastic BEM–FEM code in which the coupled hydrodynamic–structural analyses are considered. The prepared code implements an iteration approach to predict the deformed shape of the propeller. The hydrodynamic force is calculated by modelling the solid–fluid interaction in the BEM code. The deformation of the propeller is then determined using finite element software.

In the case study, a composite propeller of five blades is chosen to study the effect of the deformation on the propeller's performance. The analyses are carried out for four skew angles at advance velocity ratios of 0.2–0.9. The variations in the propeller's characteristics relative to those of the undeformed blade are defined to examine the effect of the skew angle on the hydrodynamic characteristics. The following results can be extracted from the analyses.

1. The maximum value of the principal stress occurs for a skew angle of 25° .
2. For all skew angles, when the advance velocity ratio increases, the maximum deflection, the thrust coefficient and the torque coefficient decrease.
3. The maximum value of the efficiency shifts to a slightly higher advance velocity ratio as the skew angle decreases.
4. The deformation has the least effect on the propeller's performance at $\theta_{sp} = 25^\circ$ and the greatest effect at $\theta_{sp} = 55^\circ$.
5. ΔK_{Tr} , ΔK_{Qr} and $\Delta\eta_r$ are approximately constant at $\theta_{sp} = 25^\circ$. This means that the deformation of the propeller is independent of the advance velocity ratio at $\theta_{sp} = 25^\circ$.
6. For $\theta_{sp} \leq 25^\circ$, ΔK_{Tr} and ΔK_{Qr} are negative while, for $\theta_{sp} > 25^\circ$, these parameters are positive.
7. For $J < 0.6$, $\Delta\eta_r$ is negative for $\theta_{sp} \leq 25^\circ$ and positive for $\theta_{sp} > 25^\circ$; however, for $J > 0.6$, the opposite situation occurs.

It is proposed to compare these results with the measurement data from a full-scale or model test in future work.

Funding

This research received no specific grant from any funding agency in the public, commercial or not-for-profit sectors.

References

1. Hirdaris SE and Temarel P. Hydroelasticity of ships: recent advances and future trends. *Proc IMechE Part M*: *J Engineering for the Maritime Environment* 2009; 223(3): 305–330.
2. Carlton JS. *Marine propeller and propulsion*. 2nd edition. Oxford: Butterworth–Heinemann, 2007.
3. Sontvedt T. Propeller blade stress application of finite element methods. *Comput Structs* 1974; 4: 193–204.
4. Young YL. Hydro-elastic behavior of flexible composite propellers in wake inflow. In: *16th conference on composite materials (ICCM)*, Kyoto, Japan, 8–13 July 2007, pp.1–6.
5. Young YL. Fluid–structure interaction analysis of flexible composite marine propellers. *J Fluids Structs* 2008; 24: 799–818.
6. Young YL and Savander BR. Numerical analysis of large-scale surface-piercing propellers. *Ocean Engng* 2011; 38(13): 1368–1381.
7. Blasques JP, Berggreen C and Andersen P. Hydro-elastic analysis and optimization of a composite marine propeller. *Mar Structs* 2010; 23(1): 22–38.
8. Lin HJ, Lai WM and Kuo YM. Effect of stacking sequence on nonlinear hydro-elastic behaviour of composite propeller. *J Mech* 2010; 26(3): 293–298.
9. Mulcahy NL, Prusty BG and Gardiner CP. Hydro-elastic tailoring of flexible composite propellers. *Ships Offshore Structs* 2010; 5(4): 359–370.
10. Chau TB. 2-D versus 3-D stress analysis of a marine propeller blade. *Zesz Nauk Akad Morskiej Gdyni* 2010; 64: 117–125.
11. Koronowicz T, Krzemianowski Z, Tuszkowska T and Szantyr JA. A complete design of ship propellers using the new computer system. *Pol Marit Res* 2009; 16(59): 29–34.
12. Ghassemi H and Ghadimi P. Computational hydrodynamic analysis of the propeller–rudder and the AZIPOD systems. *Ocean Engng* 2007; 34: 117–130.
13. Ghassemi H. The effect of wake flow and skew angle on the ship propeller performance. *Scientia Iranica* 2009; 16(2): 149–158.
14. Ghassemi H. Hydrodynamic performance of coaxial contra-rotating propeller (CCRP) for large ships. *Pol Marit Res* 2009; 16(59): 22–28.
15. Ghassemi H. Hydrodynamic characteristics of the surface-piercing propellers for the planing craft. *J. Mar Sci Applic* 2008; 7: 147–156.
16. Ojeda RG, Prusty B and Salas M. Finite element investigation on the static response of a composite catamaran under slamming loads. *Ocean Engng* 2004; 31: 901–929.

Appendix I

Notation

C_f	frictional coefficient
[C]	damping matrix
D	propeller diameter
\vec{D}_F	drag force acting on dr of the blade
E	modulus of elasticity
\vec{F}	total force acting on dr of the blade
$\{F_{ce}\}$	centrifugal force vector
$\{F_g\}$	force vector for each element due to gravity
$\{F_P\}$	sum of the hydrodynamic and hydrostatic force vectors
G	shear modulus of elasticity

H	depth of the hub below the free surface	x	non-dimensional radius = r/R
J	advance velocity ratio	Y_{CE}	position of the element centre in Y direction
K_Q	torque coefficient	α	angle of attack
K_T	thrust coefficient	β_i	hydrodynamic pitch angle
$[K]$	stiffness matrix	Γ	circulation
\vec{L}_F	lift force acting on dr of the blade	ΔK_{Qr}	relative variation in the torque coefficient
$[M]$	structural mass matrix	ΔK_{Tr}	relative variation in the thrust coefficient
n	rotational speed of the propeller	$\Delta \eta_r$	relative variation in the efficiency
\vec{n}	normal vector of the element surface with the components (n_x, n_y, n_z)	ε	strain
P	total pressure of each element	η	efficiency of the propeller
P_h	hydrodynamic pressure	$\theta_s(x)$	skew angle at a particular radial section
P_0	atmospheric pressure	θ_{sp}	propeller skew angle
Q	torque of the propeller	ν	Poisson's ratio
r_e	radial position of the centre of the element	ρ	density of water
T	total thrust of the propeller	ρ_b	density of the blade
\vec{u}_a	axial induced velocity	σ	stress
\vec{u}_t	tangential induced velocity	τ	tangential stress
$\{u\}$	displacement vector	φ	geometric pitch angle
$\{\dot{u}\}$	velocity vector	$\vec{\omega}$	rotational speed (rad/s)
$\{\ddot{u}\}$	acceleration vector	$\nabla\phi$	derivative of the velocity potential
\vec{V}_A	advance velocity		
\vec{V}_R	inflow velocity vector		